Catalysis Letters (2025) 155:8
https://doi.org/10.1007/s10562-024-04834-4

Plasma-Synthesized Combined Nitrogen and Cationic Species Doped-MnO_2: Impact on Texture, Optical Properties, and Photocatalytic Activity

Franck W. Boyom-Tatchemo[1,2] · Albert Poupi[2] · François Devred[1] · Elie Acayanka[2] · Georges Kamgang-Youbi[2] · Carmela Aprile[3] · Samuel Laminsi[2] · Eric M. Gaigneaux[1]

Received: 30 March 2024 / Accepted: 9 September 2024

Abstract

This work explored the possibility of doping MnO_2 structure simultaneously by cationic (Na^+, Mg^{2+} or K^+) and nitrogen species during its synthesis through gliding arc plasma route. Therefore, $NaMnO_4$, $Mg(MnO_4)_2$ or $KMnO_4$ precursor has been precipitated via plasmachemical reduction thanks to NO· and NO_2^- respectively being short and long-lived species generated in plasma plume (gas phase) and plasma post-discharge (liquid phase). Physicochemical characterizations revealed nanostructured NaN–MnO_2, MgN–MnO_2 and KN–MnO_2 respectively with specific surface areas of 36, 110 and 116 m^2/g, nitrogen atomic loading at surface of 0.6, 1.0 and 1.5%, and band gap values of 1.20, 1.30 and 1.45 eV. The three precursors with different cationic species allowed different nitrogen loading for their respective plasma-synthesized MnO_2, which led to the different values of band gap energy. An increase of the N-loading induced an increase of band gap energy and enlarged the absorption capability of MnO_2 from visible light to the UV region. Solar photocatalytic removal of TY revealed bleaching degrees of 53, 97 and 94% respectively for NaN–MnO_2, MgN–MnO_2 and KN–MnO_2 materials. This enlargement, together with the increased specific surface area of the plasma-synthesized N–MnO_2, led synergistically to an enhancement of its photocatalytic activity. This work highlights the usefulness of the synthesis via glidarc plasma, without any additional reagent, of MnO_2, as allowing cationic species insertion in their structure, and simultaneously their doping with different N-loading, so leading to different crystalline structures, and photocatalytic activities.

✉ Franck W. Boyom-Tatchemo
boyom.william@yahoo.com

✉ Eric M. Gaigneaux
eric.gaigneaux@uclouvain.be

[1] Division Molecular Chemistry, Materials and Catalysis (MOST), Institute of Condensed Matter and Nanosciences (IMCN), UCLouvain, Place Louis Pasteur 1, Box L4.01.09, B-1348 Louvain-La-Neuve, Belgium

[2] Inorganic Chemistry Department, University of Yaoundé I, P.O. Box 812, Yaoundé, Cameroon

[3] Laboratory of Applied Materials Chemistry, Unit of Nanomaterials Chemistry, Chemistry Department, University of Namur, NISM, Rue de Bruxelles, 61, 5000 Namur, Belgium

Published online: 11 November 2024

Graphical Abstract

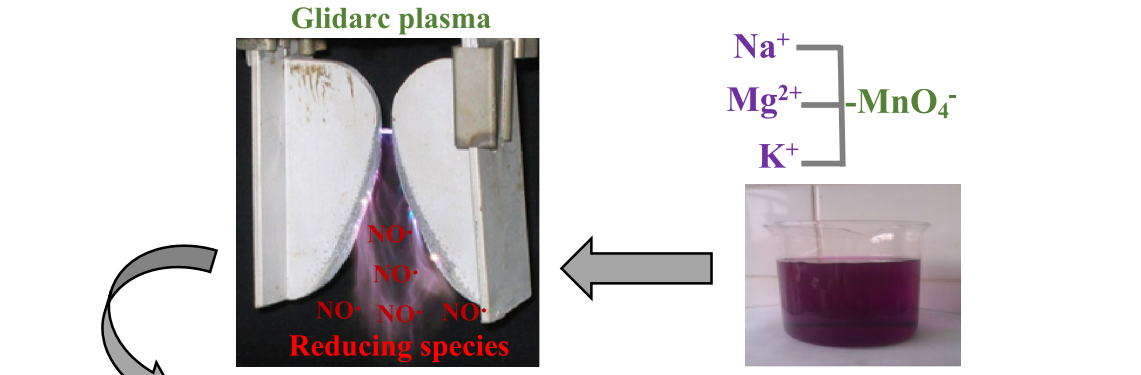

Material	Cationic diameter (Å)	Specific surface area m^2/g	%N (at)	Band gap (eV)	%Bleaching TY
NaN-MnO_2	**Na^+ (2.04)**	36	0.6	1.20	53
MgN-MnO_2	**Mg^{2+} (1.32)**	110	1.0	1.30	97
KN-MnO_2	**K^+ (2.66)**	116	1.5	1.45	94

Keywords Glidarc plasma · N-doping MnO_2 · Cationic-doped MnO_2 · Photocatalytic depollution

1 Introduction

Many research works showed that semiconductors nanomaterials surface such as TiO_2, ZnO, NiO and MnO_2 are photosensitive to solar light. As a result, these semiconductors can be used as photocatalysts for degradation of large organic pollutants [1–4]. Heterogeneous solar photocatalysis appears as an ecological technology for the removal of pollutants, based on various advantages such as free solar energy, ambient temperature, and use of dissolved oxygen as an oxidizing agent [3, 5]. Herein, we focus our attention on MnO_2 as promising material, considering its high catalytic activity, low cost, low toxicity, and environmental friendliness [6–8]. However, MnO_2 nanomaterials show some drawbacks. Firstly, the use of MnO_2 is limited by its instability owing to structural degradation during many applications cycling, which could induce its leaching [9]. Secondly, MnO_2 has a narrow band gap energy, which significantly limiting its photoactivity in the visible light region [10]. It becomes interesting, even timely, to improve the photosensitivity of nanomaterial in the solar light to ensure its good reactivity. Doping is one of the important methods of physicochemical properties modification of functional materials. Thereby, the synthesis of transition metal oxide nanomaterials with high activity, stability and long-life cycle is a necessity, to ensure their efficiency and profitability for various industrial uses, such as energy storage, photo(catalysis) and also environmental depollution [11–13]. To solve the problem of MnO_2 stability during its applications, Kalhor et *al.* (2021) stabilized MnO_2 nanoparticles on Zeolite-NaY and prevented the leaching process during many cycles of catalytic reactions [14]. Cojocaru et *al.* (2009) reported that the synthesis procedure significantly influences the band gap value, through the insertion of impurities in the crystalline structure of the semiconductor and established a good correlation between the band gap value and the photocatalytic activity [15]. Aprile et *al.* (2008) reported a contradiction on an increase or a decrease of the (photo)catalytic activity after metal doping, which controversial results depend on the method by which the metal has been introduced and on the concentration of dopants [16].

Herein, we intend to improve the photocatalytic efficiency of gliding arc plasma-synthesized MnO_2 and its stability (structural and photocatalytic), by simultaneously nitrogen-doping and inserting cationic species (Na, Mg, and K). Various polymorphs of MnO_2 have been doped by chemical elements including Cerium (Ce), Cobalt (Co), Gold (Au), and Bismuth (Bi), during their syntheses via conventional processes such as hydrothermal and co-precipitation, which require long preparation times and high temperature, thus involving expensive costs [17–20]. Moreover, with certain methods, doping element of MnO_2 comes from another

reagent added to the synthesis precursor, which may perturb the system. Gliding arc plasma route appears as an innovative, versatile, and ecological process for MnO_2 nanomaterial synthesis through HO· or (NO· and NO_2^-) species respectively as oxidizing or reducing species [21–23]. Poupi et *al.* (2018) reported that photocatalytic properties of TiO_2 nanoparticles could be improved by nitrogen doping through nitrogenous species generated in glidarc plasma medium [24]. Thereby, we here wonder whethervarious polymorphs of MnO_2 could be doped simultaneously by cationic and nitrogen species during their synthesis via glidarc plasma route without any supplementary reagent, while using the cation from the precursor.

In this work, we explore on the one hand, the insertion of nitrogen and cationic species within the MnO_2 lattice via plasma-reduction process, in order to increase its photoactivity under solar light irradiation, through an efficient generation and separation of photogenerated electron–hole pairs, and their migration to the reaction medium. On the other hand, we explore the impact of cationic species on nitrogen loading within plasma-synthesized MnO_2, the relationship between band gap (optical property), specific surface area (textural property) and photocatalytic activity. Therefore, solutions of permanganate with different cationic species (Na^+, K^+ or Mg^{2+}) have been exposed to gliding arc plasma discharge, to allow the doping of their structures. Materials obtained were characterized via XRD, Raman, FTIR, XPS, N_2 physisorption, UV–Vis and SEM analyses, and their photocatalytic activities measured in the bleaching/degradation of Tartrazine Yellow (TY) as an organic pollutant.

2 Experimental Strategy

2.1 Gliding arc Plasma as Synthesis Device

Figure S_1 represents the scheme of gliding arc plasma as experimental synthesis device available in laboratory of heterogeneous catalysis, IMCN, MOST, Université catholique de Louvain, Belgium. Briefly, the feeding gas, i.e. atmospheric air (H_2O, N_2, O_2) is supplied (450 L/h) by an air compressor. This air passes through a bubbler containing de-ionized water, where it is humidified before being injected along the stainless-steel electrodes through a nozzle. The electrodes are connected to a high voltage transformer (AC 240 V/4.5 Kv–4.31A) which delivers a mean current intensity of 130 mA, and a voltage of 2400 V (312 W), in operating conditions. Then, an electric arc is formed at the smallest electrodes gap, when the high voltage is applied. This arc is pushed away by air-flow (450 L/h) from the nozzle and glides along the electrodes, until it collapses. A new arc then forms and the cycle restarts forming a large plasma plume in contact with the liquid surface. The nozzle diameter and the gap between the electrodes (in stainless-steel) are 1 and 2 mm respectively. The electrodes length is cm and distance between the bottom of electrodes and the surface of target solution is 2–3 cm.

2.2 Synthesis Procedure

Precursors used were $KMnO_4$ (99% wt Roth company), $NaMnO_4$ (40% wt in H_2O, Sigma-Aldrich) and $Mg(MnO_4)_2$ (Sigma-Aldrich). The target solutions of each precursor (450 mL, 700 mg/L) prepared with de-ionized water, were exposed to plasma discharge under magnetic stirring, until complete precipitation (Fig. 1). The brown-black precipitate obtained was recovered by simple filtration, washed several times with de-ionized water and dried in oven at 105 °C under air. Equations (1–5) illustrate the set of reactions proceeding, with in particular Eq. 5 showing the plasmachemical reduction of $KMnO_4$, $NaMnO_4$ or $Mg(MnO_4)_2$ by NO· as being a short-lived species generated in plasma plume (gaseous phase) [21, 22]. It must be noted that other species such as NO_2^-, known as long-lived species, generated in plasma post-discharge (solution phase), also allow the plasma-reduction of MnO_4^- (Eq. 7) [23]. The reproducibility of the synthesis product after many batches is ascertained by the fact that the operating synthesis remains unchanged.

$$H_2O + e^- \rightarrow H^{\cdot} + HO^{\cdot} + e^- \quad (1)$$

$$H_2O + e^- \rightarrow H^+ + HO^{\cdot} + 2e^- \quad (2)$$

$$O_2 + e^- \rightarrow 2O^{\cdot} + e^- \quad (3)$$

$$N_2 + O^{\cdot} \rightarrow NO^{\cdot} + N^{\cdot} \quad (4)$$

$$MnO_4^- + NO^{\cdot} \rightarrow MnO_2 + NO_3^- \quad (5)$$

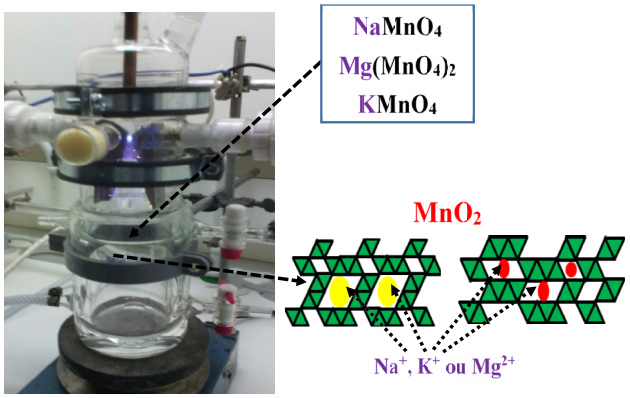

Fig. 1 Picture of gliding arc plasma-reduction of different solutions of cation-MnO_4

$$NO_2 + e^- \rightarrow NO_2^- \quad (6)$$

$$MnO_4^- + 4H^+ + 3NO_2^- \rightarrow MnO_2 + 3NO_2 + 2H_2O \quad (7)$$

2.3 Characterization Techniques

X-ray diffraction patterns of the different materials were recorded between angle values 2θ = 5° and 80° at the rate of 0.6°/min with an increment of 0.02° and an integration time of 2 s using a D8 ADVANCE BRUKER diffractometer, operating at 40 kV and 40 mA, with the Cu K_α radiation (1.5418 Å). The powdered samples previously ground, were deposited on disks slightly impregnated with handcream. Detection is performed using a LynxEye XE-T Technology detector. The ICDD-JCPDS database was used to identify the crystalline phases. Raman spectroscopy was carried out using a Bruker RFS 100IS, equipped with a 532 nm excitation laser (10 mW), and working with 4 cm^{-1} as resolution. Raman spectra were collected after 5 scans using a confocal spectrometer, with a magnification objective of 10x, a spot size of 100 microns; acquisition time was 15 s. Fourier transform infrared spectroscopy was recorded in transmission mode after 100 scans, at a resolution of 4 cm^{-1}, with an Equinox IFS55 spectrometer (Bruker) equipped with a DTGS detector. The pellets were made by diluting the samples in KBr (2 mg of sample for 200 mg of KBr), and then pressing them into self-supporting disks using a hydraulic press (5–7.5 bar) for about 5 min. The atmospheric air spectrum has been used as a reference and subtracted from the spectra. X-ray photoelectron spectroscopy was carried out using an Axis Ultra (SSX-100/206) spectrometer equipped with a 30° solid acceptance lens, a hemispherical analyser, and a monochromatic source of Al K_α (1486.6 eV) operated at 15 kV and 10 mA. The pressure within the analysis chamber was about 10^{-6} Pa. The angle between the surface normal and the axis of the analyser lens was 55°. The analysed area was approximately 1.4 mm^2 and the pass energy was set at 150 eV. In these conditions, the full width at half maximum (FWHM) of the Au $4f_{7/2}$ peak of a clean gold standard sample was about 1.6 eV. A flood gun set at 8 eV and a nickel (Ni) grid placed 3 mm above the sample surface were used for charge stabilisation. The sample powder was pressed in small stainless-steel troughs of 4 mm diameter and placed on an aluminium conductive carousel. Before analysis, all samples were outgassed beforehand under vacuum (10^{-5} Pa) for 24 h to remove the physisorbed compounds. The binding energy scale was calibrated by taking the carbon C1s peak fixed at 284.8 eV (aliphatic component of carbon contamination) as reference. Atomic ratios were obtained using peak areas normalized based on acquisition parameters and experimental sensitivity factors provided by the manufacturer. The Mn2p region was used to quantify Mn proportion. Proportions of lattice oxygen (structural) and chemisorbed oxygen (surface) were decomposed from the O1s signal after deducing the oxygen-related to contamination carbon. The Mn average oxidation state (AOS) was determined using the difference of the Mn3s binding energy with that of its satellite [25, 26], following Eq. 8 [27].

$$AOS = 8.956 - 1.126\,\Delta E_s \quad (8)$$

where ΔE_s represents the difference of binding energy between Mn3s and its satellite.

Nitrogen physisorption was carried out at −196 °C using a Micromeritics Tristar 3000 in the relative pressure range [10^{-6}-0.99]. Before analysis, 150 mg of sample was outgassed at 150 °C for 12 h under primary vacuum (about 10 mbar). In practice, the weighed ground sample is introduced into glass tubes with a filler rod to limit the error made on the measurement due to the dead volume of the glass tubes. The specific surface area, and total pore volume (pore size distribution) were calculated using Brunauer–Emmett–Teller (BET) equation in the 0.05–0.30 p/p^0 range and the Barrett-Joyner-Halenda (BJH) method respectively. Error on the specific surface area was determined by calculating the standard deviation on a series of values related to 3 analyses of the same sample. The morphology was investigated using a LEO 983 GEMINI electron microscope operated at an acceleration voltage between 10 and 15 kV depending on the samples. Before analysis, the samples were metalized under argon atmosphere with an about 15 nm thick layer of chromium under vacuum with a Sputter Metal 208HR (Cressington). The optical properties of plasma-synthesized MnO_2 have been explored using diffuse reflectance UV–VIS spectroscopy analysis within the region 200–800 nm with the Cary Win UV software package and a CARY 5000 Agilent Spectrophotometer equipped with a praying Mantis available in Laboratory of Applied Materials Chemistry, University of Namur, Belgium. A $BaSO_4$ pellet was used as a blank, and the Kubelka–Munk function was used to calculate the band gap energy by plotting $(F(r)*E)^{1/2}$ versus energy of light.

2.4 Solar Photocatalytic Bleaching Processes of Tartrazin Yellow Dye

Tartrazin Yellow (> 97%) was purchased at Sigma-Aldrich company. Photocatalytic experiments were performed in the presence of solar light, with a TY solution (40 mg/L, pH = 2.5) and a catalyst mass of 100 mg. All experiments were carried out at ambient temperature in Belgium (summer season) between June and July 2019, within a batch reactor exposed to solar light, whose average intensity

measured using a digital lightmeter is about 5.25 kW h/m^2, with an error of 5%. Residual concentration of TY was analysed with a GENESYS 10S Vis spectrophotometer at 425 nm. The bleaching degree (%D) was calculated using Eq. 9, where C_0 and C_t represent respectively initial and residual concentrations of TY at defined times.

$$\%D = \left[\left(C_0 - C_t\right)/C_0\right]100 \quad (9)$$

3 Results and Discussion

3.1 Structural Analysis

Figure 2 depicts XRD patterns of materials obtained after exposure of $NaMnO_4$ (Fig. 2a), $Mg(MnO_4)_2$ (Fig. 2b) and $KMnO_4$ (Fig. 2c) to plasma plume. The three patterns reveal diffraction peaks at 12.5°, 19.8°, 22.6°, 33°, 37°, 38°, 42.5°, 49°, 56.2°, 60.5°, 65.3° and 67.8° which are ascribed to γ-MnO_2 (JCPDS 14-0644) [28, 29] and α-MnO_2 (JCPDS 44-0141) [30, 31], illustrating a mixture of two polymorphs. The large peaks at 22.5° and 56.2° reveal a significant presence of γ-MnO_2 polymorph compared to α-MnO_2 polymorph. The peaks at 12.5° and 19.8° illustrate the insertion of Na^+ (2.04 Å) [32], Mg^{2+} (1.32 Å) [32] and K^+ (2.66 Å) [31] species within 4.6Å × 4.6 Å tunnels of α-MnO_2 polymorph [33]. However, considering the size of 2.3Å × 2.3 Å and 2.3Å × 4.6 Å tunnels of γ-MnO_2 polymorph, only Na^+ (2.04 Å) and Mg^{2+} (1.32 Å) are likely to fit into the structure of this polymorph [29]. Therefore, each of our three prepared materials are made of two polymorphs: α-MnO_2 (named Cryptomelane, with tunnels structure) and γ-MnO_2 (named Nsutite, with tunnels structure) each in different proportion following the difference of the peak intensity on the three patterns. The plasma-reduction of the three permanganate solutions under operating conditions of 312W (power, 130 mA, 2400 V), 450 L/h (airflow), after 15 min, revealed products composed of two polymorphs, namely α-MnO_2 and γ-MnO_2 (Fig. 3). In our previous work, we reported obtaining of α-MnO_2 after 28 min of plasma-reduction of $KMnO_4$ solution under operating conditions of 96W (160 mA, 600 V) and 800 L/h [22]. These results, summarized on Fig. 3, show that power and airflow significantly impact the nucleation time, thus the nature of polymorphism and moreover highlight the effect of plasma parameters on the nature of obtained products. Boyom et *al.* (2020) show that changing the voltage or airflow during plasma-reduction or oxidation of Mn solution could changes the polymorph [22]. Therefore, in the present work, the obtaining of mixture of polymorphs at 312W could be attributed to a high reactivity, in the meaning that the first precipitated α-MnO_2 are converted to γ-MnO_2 through ageing (maturation) process. Boyom et *al.* (2021) also reported a conversion of plasma-precipitated α-MnO_2 to γ-MnO_2 after ageing at temporal post-discharge [34].

Raman spectra of the three materials are represented on Fig. 4. A large and intense peak at 632 cm^{-1} is observed, being ascribed to the vibrations of Mn–O bond within MnO_6 octahedron of γ-MnO_2 [35]. A peak shoulder at 558 cm^{-1} on Mg–MnO_2 (Fig. 4b) and K–MnO_2 (Fig. 4c) spectra, illustrates the significant presence of α-MnO_2 within both materials [36]. Therefore, this analysis confirms the presence of the two polymorphs (Cryptomelane and Nsutite structures) components in each of the three prepared materials. However, this peak shoulder is only slightly noticeable on Na–MnO_2 spectrum (Fig. 4a) which attests the weak presence of α-MnO_2 compared to Mg–MnO_2 and K–MnO_2. Figure 5 shows FTIR spectra of obtained MnO_2, which reveal absorption bands at 3420, 1620 and 1085 cm^{-1} characterizing the stretching and bending vibrations of H–O bond of physisorbed water. The slightest peak at 1380 cm^{-1} illustrates a weak presence of chemisorbed or crystallization water within the three materials [37]. Absorption

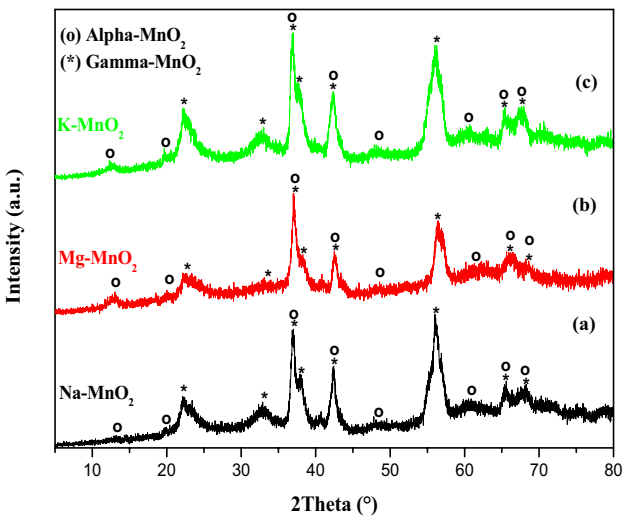

Fig. 2 XRD patterns of plasma-synthesized N–MnO_2

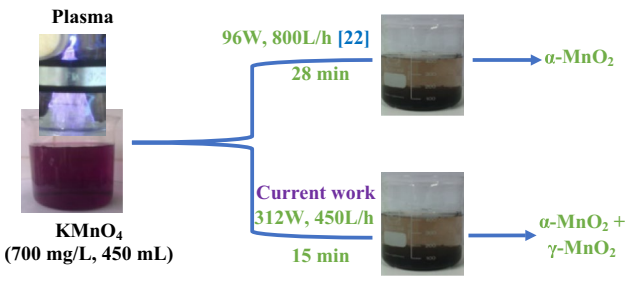

Fig. 3 Effect of plasma power supplied on the exposure time and crystalline structure of plasma-synthesized N–MnO_2

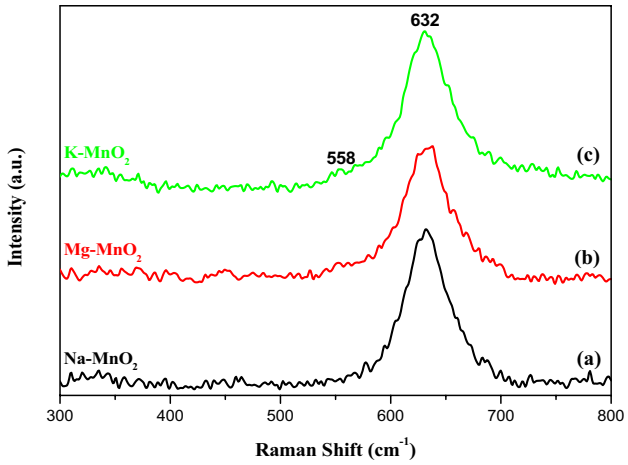

Fig. 4 Raman spectra of plasma-synthesized N–MnO_2

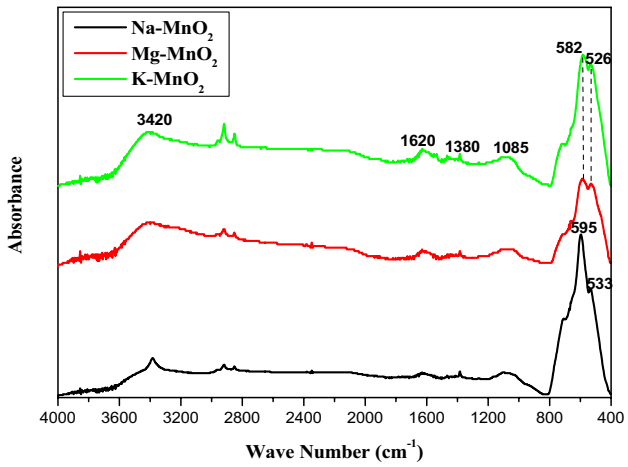

Fig. 5 FTIR spectra of plasma-synthesized N–MnO_2

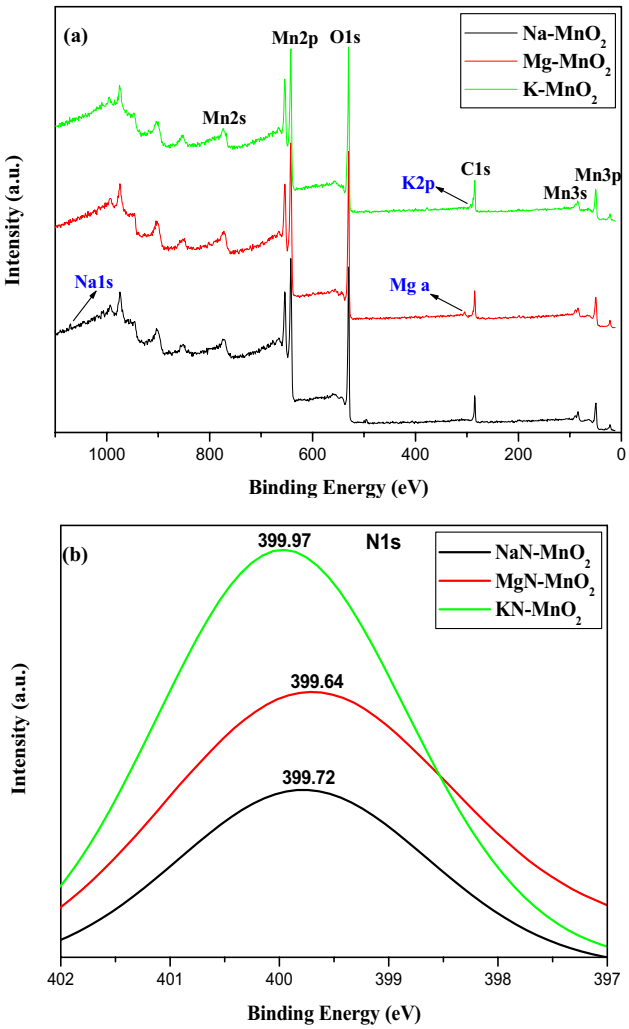

Fig. 6 **a** XPS spectra and **b** Nitrogen region of plasma-synthesized N–MnO_2

bands within the wavelength range of 800–400 cm^{-1} are ascribed to the stretching vibrations of Mn–O bond within MnO_6 octahedron of the different oxides [37, 38]. However, Mg–MnO_2 and K–MnO_2 show similar peaks at 582 and 562 cm^{-1}, whose explanation could be a more important presence of α-MnO_2 within Mg–MnO_2 and K–MnO_2 than in Na–MnO_2, as previously revealed via XRD and Raman analyses.

3.2 Surface, Morphological and Optical Analyses

To have a deeper insight on cationic and nitrogen species doping each MnO_2, X-ray photoelectron spectroscopy (XPS) analysis has been carried out. Figure 6a reveals Na, Mg and K elements and highlights the insertion of these elements within their respective plasma-synthesized MnO_2. Table 1 shows XPS data of the three MnO_2, with Mn appearing in mixed valence (III, IV) according to their respective Mn average oxidation state (AOS) values. We recorded identical values of atomic ratio (Mn/O) within these materials, despite the difference of cationic size species which compose these MnO_2. This is in line with the mixed crystalline structure found to be identical in the three MnO_2. Besides, the almost identical value of chemisorbed oxygen (O_α) for the different MnO_2 could be explained by the identical nature of polymorphs components. K–MnO_2 material shows an oxygen lattice (O_β) fraction lower than those of Na–MnO_2 and Mg–MnO_2. Thus, the larger K^+ ion (2.66 Å) would induce more loss of lattice oxygen compared to smaller Na^+ (2.04 Å) and Mg^{2+} (1.32 Å) ions. These results could attest the presence of different cationic species within the lattice of the prepared materials. The chemical state of nitrogen within the three plasma-synthesized MnO_2 has also been investigated through XPS (Fig. 6b). The three materials show N1s peaks at binding energies values: KN–MnO_2 (399.97 eV),

Table 1 XPS data of plasma-synthesized N–MnO_2

Material	AOS (Mn)	%N (atom)	%Metal (atom)	Mn/O	$\%O_\alpha$	$\%O_\beta$	O_α/O_β
NaN–MnO_2	3.46	0.6	Na/1.2	0.46	12.3	38.8	0.32
MgN–MnO_2	3.31	1.0	Mg/0.8	0.46	11.7	38.3	0.31
KN–MnO_2	3.43	1.5	K/1.1	0.46	11.4	34.8	0.33

MgN–MnO_2 (399.64 eV) and NaN–MnO_2 (399.72 eV) which could be ascribed to anionic N^- incorporated within the MnO_2 lattice through substituting oxygen atoms and could be in the form of N–Mn–O [2, 39], knowing that NO_2^- and NO_3^- are generated in gliding arc plasma medium with humidified atmospheric air as feeding gas [21, 22]. The higher binding energy value of nitrogen within KN–MnO_2 compared those within NaN–MnO_2 and MgN–MnO_2 (almost the same) could be explained by the difference of oxidation state of nitrogen within these materials. Therefore, the oxidation state of nitrogen within KN–MnO_2 is higher than that within NaN–MnO_2 and MgN–MnO_2. In addition to the single substitution of oxygen through establishment of N–Mn–O bond within the three, we could envisage a double substitution of oxygen through N–Mn–N within KN–MnO_2 which would be in line with the highest binding energy of nitrogen component in this material. The nitrogen loading value within each material (Table 1) follows an evolution as NaN–MnO_2 < MgN–MnO_2 < KN–MnO_2. We would have expected to have a higher nitrogen loading within MgN–MnO_2 than KN–MnO_2 referring to the lower cationic diameter of Mg compared to those of K and Mn. Thereby, after Mg substitution with the MnO_2 lattice, there would be more space released allowing more incorporation of nitrogen at interstitial positions. Otherwise, the three materials have the same values of Mn/O and O_α/O_β ratio, thus illustrating a regular oxygen substitution, and probably an irregular nitrogen incorporation within the generated interstitial.

Adsorption–desorption isotherms of the different MnO_2 are depicted on Fig. 7. They all present a hysteresis loop, between type IV adsorption and desorption relatively parallel isotherms, which is typical of mesoporous materials with pores open at both sides [37]. Besides, NaN–MnO_2 material shows narrow hysteresis loop at relatively high partial pressure [0.9–1.0], attesting its low mesoporosity, but high macroporosity [40]. As a counterpart, KN–MnO_2 reveals the largest mesoporosity, while MgN–MnO_2 shows intermediate features. Table 2 summarizes the textural data of the three materials and reveals a higher specific surface area for K–MnO_2 and Mg–MnO_2 than Na–MnO_2. This could be ascribed, on the one hand, to the more marked presence of α-MnO_2 with 4.6Å × 4.6 Å tunnels developing more pores within K–MnO_2 and Mg–MnO_2. Figure 8 shows SEM images which reveal agglomerated particles with irregular morphology for all obtained Na–MnO_2 (Fig. 8a), Mg–MnO_2 (Fig. 8b), and K–MnO_2 (Fig. 8c). Therefore,

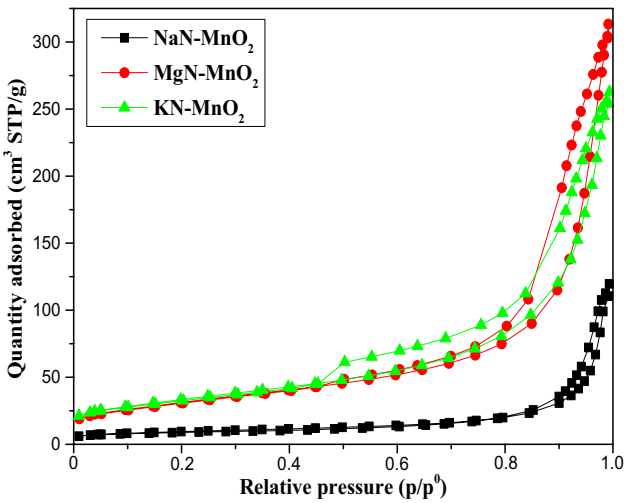

Fig. 7 Adsorption–desorption isotherms of plasma-synthesized N–MnO_2

Table 2 Textural and optical data of plasma-synthesized N–MnO_2

Material	Specific surface area (m^2/g)	Pores diameter (nm)	Pores volume (cm^3/g)	Eg (eV)
NaN–MnO_2	36 ± 3	25	0.15	1.20
MgN–MnO_2	110 ± 8	14	0.45	1.30
KN–MnO_2	116 ± 8	11	0.38	1.45

cationic species difference does not affect the morphology of the three N-doped samples. This unchanged morphology, which is like crystalline structure revealed by XRD, could be explained by fact that, the plasma-reduction of main permanganate ion (MnO_4^-) component the three precursors, follow the same nucleation process of the crystallites, despite their different cationic metal.

Figure 9a depicts the UV–Vis reflectance spectra of the plasma-synthesized MnO_2. The band gap (E_g) values recorded through Kubelka–Munk function (Fig. 9b) are 1.20, 1.30 and 1.45 eV respectively for NaN–MnO_2, MgN–MnO_2 and KN–MnO_2. Knowing that nitrogen (N) atom gets five valence electrons, it can form four covalent bonds with Mn, thus there remains one free electron which can participate to the electric conduction by affecting the band gap energy. Nitrogen atom as electron donor, induces a type-n doping.

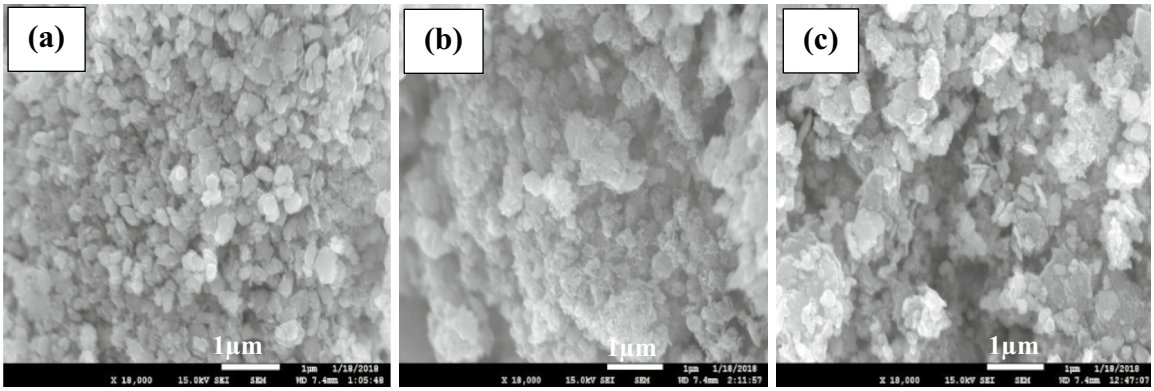

Fig. 8 SEM images (×18,000) of plasma-synthesized **a** NaN–MnO_2, **b** MgN–MnO_2 and **c** KN–MnO_2

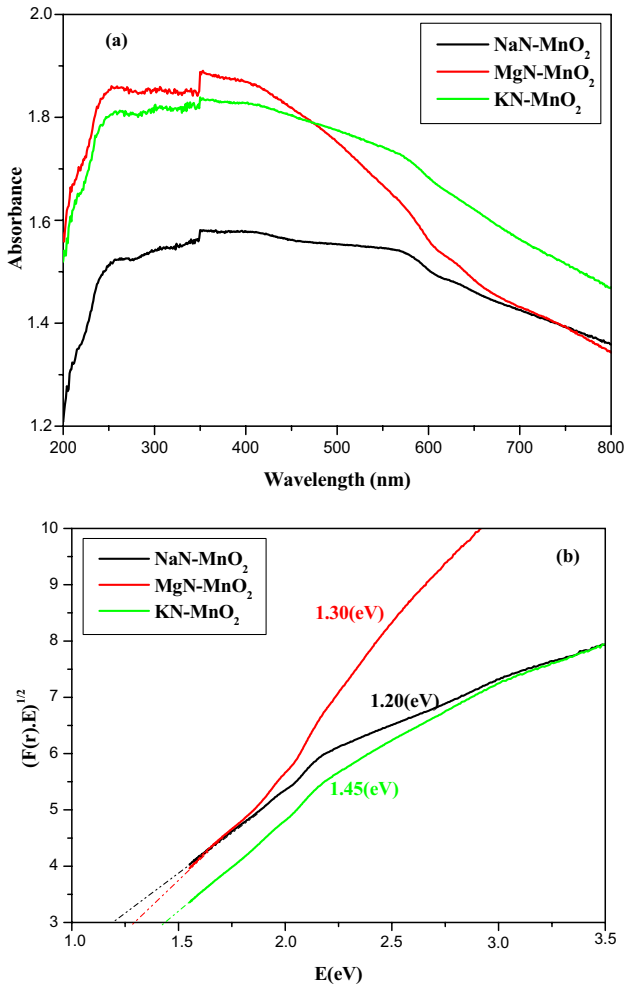

Fig. 9 **a** UV–Vis spectra of plasma-synthesized N–MnO_2, **b** Normalized Kubelka–Munk functions

Therefore, introduction of nitrogen atom as foreigner element in large quantity within the structure of MnO_2 semiconductor, significantly affects the band gap energy value. Accordingly, the fact that the three synthesis precursors differ by their cationic species (with different sizes) inserted within their MnO_2 lattice, leads to different nitrogen loading. This result reveals the fact that an increase of N-doping induces a raise of the band gap energy (Table 2), and correspondingly a restriction of the absorption range of the material. Conversely, Chen et *al.* (2011) reported that N-doped TiO_2 nanomaterial had a decreased band gap energy and exhibited high photocatalytic activity under visible-light [41]. Mahy et *al.* (2018) also showed that N-doped TiO_2 had a reduced band gap energy by creating an intermediate band for the electrons below the conduction band or above the valence band, so allowing activity in the visible range [39]. Aprile et *al.* (2013) reported the enlargement of TiO_2 photocatalytic activity from UV light to visible light through doping with metallic and non-metallic elements [16]. The question now is to know which among this augmentation of the band gap energy induced by nitrogen-doping, which could induce a reduction of absorption within visible light range by plasma-synthesized MnO_2, or another parameter such as the specific surface area, could be the predominant one on the photocatalytic process. Boyom et *al.* (2021) reported on the one hand, the decrease of the specific surface area of plasma-synthesized α-MnO_2 during ageing (plasma post-discharge reactions) at 100 °C, and on the other hand, a significant decrease of its catalytic activity compared to photocatalytic activity [42]. The authors also hypothesized that the band gap of the plasma-synthesized α-MnO_2 had not been affected during the ageing which could explain the only moderate diminution of its photocatalytic efficiency, despite the decrease of its specific surface area [42].

From all what preceeds about the physicochemical characterization of the three cation-Nitrogen doping, it is clear that preparing the MnO_2 without cationic species as reference material would allow to solidy the interpretations proposed. Unfortunately, to synthesize MnO_2 without metal cation, a precursor in which Mn is in a low oxidation state

(Mn^{2+} or Mn^{3+}) such as Mn acetate should be used in a plasma-oxidation approach, i.e. different from that used in this work namely the plasma-reduction of Mn^{7+}. The cation free MnO_2, that would be prepared would thus not be relevant for the evoked comparison.

3.3 Photocatalytic Tests

Figure 10 depicts the evolution of bleaching degree of TY during solar photocatalytic tests with the three catalysts. We observe a significant removal of TY, 25, 29 and 26% respectively for NaN–MnO_2, MgN–MnO_2 and KN–MnO_2 materials after 2 min of treatment, which could be attributed to an adsorption event, being the first step of the photocatalytic process. Thereafter, the range time of 2–60 min could be ascribed to the photocatalytic degradation of TY properly, where we record a large bleaching of TY with MgN–MnO_2 (97%) and KN–MnO_2 (94%) compared to the one obtained with NaN–MnO_2 (53%). This could be explained on the basis of the specific surface area values MgN–MnO_2 and KN–MnO_2 about three time larger than the one of NaN–MnO_2 (Table 2). However, we could not ignore the significant difference of band gap for the different samples, associated to an augmentation of nitrogen doping itself related to the presence of Mg or K. MgN–MnO_2 shows a higher bleaching degree compared to KN–MnO_2, despite the higher specific surface area of the latter compared to the one of MgN–MnO_2. This could be explained by the fact that MgN–MnO_2 has higher pore volume and diameter compared to KN–MnO_2 allowing more pollutant molecules to adsorb on its surface, thus reinforcing the photocatalytic bleaching of TY. Based on this, it is obvious that bleaching photocatalytic efficiency of TY not only is dictated by the textural parameter (Specific surface area), but also the optical parameter (Band gap). We could actually consider a synergetic effect between both parameters, through the adsorption of TY at the catalyst surface and solar light respectively controlled by the specific surface area and the band gap. To have a deep insight on the predominant parameter during the bleaching solar photocatalytic of TY, Figure S_2 highlights the bleaching degree of TY after 60 min with the three catalysts. NaN–MnO_2 with the specific surface area three times lower than those of Mg–MnO_2 and KN–MnO_2, reveals a bleaching degree higher than the half of the ones obtained with the two other catalysts. This more highlights the synergy between the specific surface area and band gap, on the one hand, and the difficulty to define the predominance of one parameter on to other (Fig. S_2 and Table S_1).

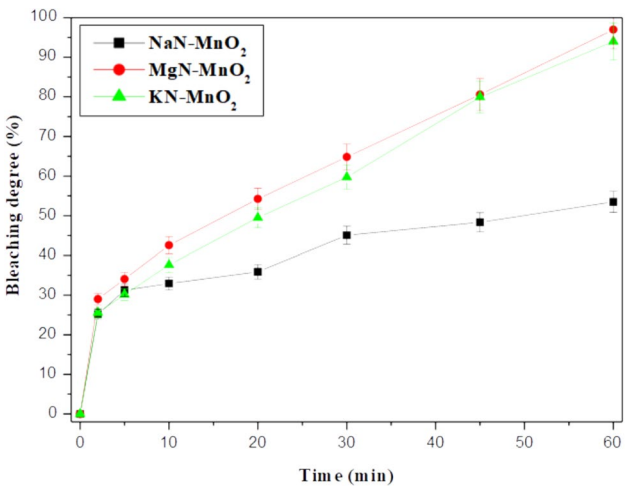

Fig. 10 Evolution of photocatalytic bleaching of TY with plasma-synthesized N–MnO_2 with exposure time

Obviously, band gap evolution (NaN–MnO_2 > MgN–MnO_2 > KN–MnO_2) should literally extend the photoactivity of MnO_2 from visible light region to UV light region, with a corresponding increase of its photocatalytic activity [39, 41]. Otherwise, MgN–MnO_2 plasma-synthesized shows a photocatalytic bleaching efficiency of 97% under operating conditions of ([TY] = 40 mg/L, pH = 2.5, [MgN–MnO_2] = 1000 mg/L, exposure time = 60 min) higher than 13% obtained by Modirshahla et *al.* (2011) with commercialized SnO_2 coupled to UV lamp under operating of ([TY] = 40 mg/L, pH = 7, [SnO_2] = 900 mg/L, exposure time = 50 min) [43], and 45% obtained by Marandi et *al.* (2013) with Clinoptilolite (local material) coupled to UV lamp under operating of ([TY] = 45 mg/L, pH = 5, [Clinoptilolite] = 40 mg/L, ([H_2O_2] = 30 mg/L, exposure time = 55 min) [44]. Figure S_3 shows UV–vis spectra evolution of TY after photocatalytic treatment with the three catalysts. The absorption bands of TY at wavelengths of 260 and 425 nm almost disappeared after 60 min of treatment with MgN–MnO_2 (Fig. S_3b) or KN–MnO_2 (Fig. S_3c) compared to NaN–MnO_2 (Fig. S_3a). However, besides the disappearance of both bands, no appearance of new bands is recorded, which attests the degradation of TY through a cleavage of nitrogen-nitrogen double bonds (–N = N–) being the chromophore group responsible of yellow colour, and degradation of the polyaromatic ring [22].

Following Fig. 10, after attributed the range time of 0–2 min to the adsorption step of TY, we have studied the kinetic photocatalytic degradation of TY with the three catalysts within the range time of 2–45 min, assuming a first order reaction (Table 3 and Fig. S_4). According to the correlation coefficient values (R^2), we observe that the photocatalytic bleaching process of TY with plasma-synthesized NaN–MnO_2, MgN–MnO_2 and KN–MnO_2 as catalysts, fits the pseudo first order kinetic, which indicates that the photobleaching of TY is dependent on its concentration in solution [42]. On the other hand, this could also be attributed to the significant generation and long lifetime of electron–hole

Table 3 Kinetic study of photocatalytic bleaching reaction of TY

Material	First order	
	R^2	K (min^{-1})
NaN–MnO_2	0.9495	0.0083
MgN–MnO_2	0.9854	0.0293
KN–MnO_2	0.9620	0.0291

pairs, leading to an efficient reaction between TY molecules and the reactive photogenerated radicals [45, 46], following the mechanism established by Modirshahla et *al.* (2011) [43], Marandi et *al.* (2013) [44], Ansari et *al.* (2024) [47] and Yadav et *al.* (2024) [48]. Reaction with MgN–MnO_2 or KN–MnO_2 is faster than with NaN–MnO_2 according to their respective kinetic constants values. This implies that nitrogen doping of MnO_2 structure significantly enhances its photocatalytic activity. Mekprasart et *al.* (2011) reported that nitrogen doped TiO_2 lattice was able of significantly improved photocatalytic degradation, due to nitrogen-induced band gap energy contraction, which improves the optical absorption of photocatalyst under visible light [49].

Recycling test of the three materials has been carried out (Fig. 11). It can be observed a quasi-constant of the photocatalytic activity of these plasma-synthesized MnO_2 during three cycles. Therefore, the photocatalytic stability of these materials could be ascribed to the cationic species (Na^+, Mg^{2+} and K^+) inserted within their respective plasma-synthesized MnO_2. Boyom et *al.* (2020) associated the high catalytic stability of plasma-synthesized α-MnO_2 during four cycles of TY bleaching, to K^+ species present in the structure of this polymorph [22]. Boyom et *al.* (2023) also reported that plasma-synthesized γ-MnO_2 without any cationic species within its channel loses its catalytic activity after one cycle [50]. To have a deep insight on the structural stability of N-doped plasma-synthesized MnO_2 during photocatalytic treatment of TY, XRD patterns of the three materials after the first cycle have been recorded (Fig. 12). We observe that the photocatalytic bleaching of TY does not affect the crystalline structure of the plasma-synthesized MnO_2, which corroborates the photocatalytic stability previously revealed.

4 Conclusion

Doping the crystalline structure of MnO_2 has been successfully performed during its synthesis via the gliding arc plasma route. Indeed, nanostructures of NaN–MnO_2, MgN–MnO_2 and KN–MnO_2 with different nitrogen loading have been plasma-synthesized, while inserting the respective cationic species within the tunnels of α-MnO_2 and γ-MnO_2 polymorphs constituting the three materials without any additional reagent. An augmentation of the N-loading induces an augmentation of the band gap energy and specific surface area of plasma-synthesized MnO_2, thus of its photocatalytic activity. Photocatalytic efficiency is attributed to a synergy between the textural parameter (specific surface area) and optical parameter (band gap). Doping of plasma-synthesized MnO_2 with nitrogen and cationic species additionally beneficially contributes to stabilize its photocatalytic activity. Otherwise, following the input energy (312W), short synthesis time (15 min) and mild operating conditions, gliding arc plasma route appears as an interesting synthesis process of doping MnO_2 nanostructures as good photocatalysts for a better wastewater treatment, and deserves more attention for its scaling in industrial applications.

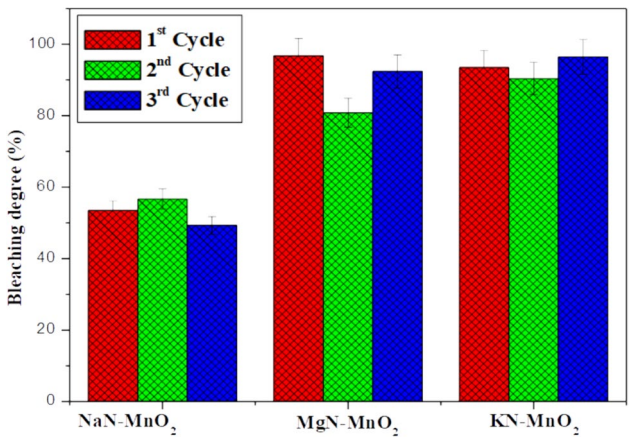

Fig. 11 Reusability of photocatalysts (N–MnO_2) during three cycles

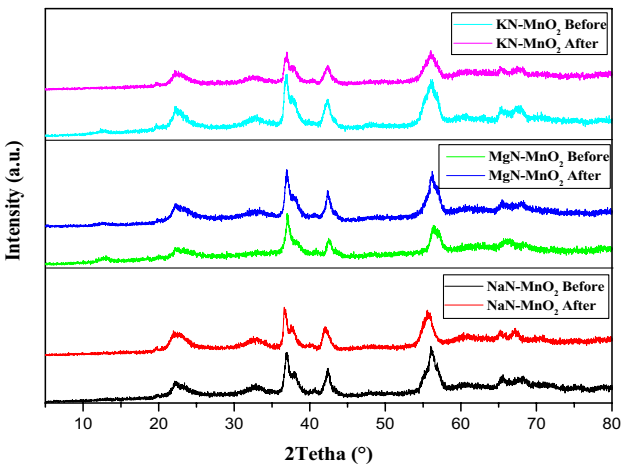

Fig. 12 XRD patterns of plasma-synthesized nitrogen and cationic-doped MnO_2 after photocatalytic test

Supplementary Information The online version contains supplementary material available at https://doi.org/10.1007/s10562-024-04834-4.

Acknowledgements The authors are grateful to the "Université catholique de Louvain" for the help awarded to carry out all this work.

Declarations

Conflict of interest Authors declare that they have no conflict of interest.

References

1. Sakthivel S, Neppolian B, Shankar MV, Arabindoo B, Palanichanry M, Murugesan V (2003) Solar photocatalytic degradation of azo dye: comparison of photocatalytic efficiency of ZnO and TiO_2. Sol Energy Mater Sol Cells 77:65–82
2. Cheng X, Yu X, Xing Z, Yang L (2016) Synthesis and characterization of N-doped TiO_2 and its enhanced visible light photocatalytic activity. Arab J Chem 9(2):S1706–S1711
3. Ansari SA (2023) Elemental semiconductor red phosphorous/ZnO nanohybrids as high performance photocatalysts. Ceram Int 49(11):17746–17752
4. Ansari SA, Parveen N, Alsulaim GM, Ansari AA, Alsharif SA, Alnahdi KM, Alali HA, Reddy VRM (2023) Emerging NiO-rGO nanohybrids for antibiotic pollutant degradation under visible light irradiation. Surf Interfaces 40:103078
5. Tang J, Zou Z, Te J (2013) Efficient photocatalytic decomposition of organic contaminants over $CaBiO_4$ under visible-light irradiation. Angew Chem Int 43:4463–4466
6. Gong W, Meng X, Tang X, Ji P (2017) Core-shell MnO_2-SiO_2 nanorods for catalyzing the removal of dyes from water. Catalysts 7(1):19
7. Bkrey IN, Monien AA (2014) Flexible laser reduced graphene oxide/MnO_2 electrode for supercapacitor applications. Int J Chem Nucl Metal Mater Eng 8:951–957
8. Umar A, Akbar S, Kumar R, Ahmed F, Ansari SA, Ibrahim AA, Alhamami MA, Almehbad N, Algadi H, Almas T, Zeng W (2024) Unveilling the potential of PANI@MnO_2@rGO ternary nanocomposites in energy storage and gas sensing. Chemosphere 349:140657
9. Purwaningrith H, Suari NMIP, Widiyastuti W, Setyawan H (2022) Preparation of Rgo/MnO_2 composites through simultaneous graphene oxide reduction by electrophoretic deposition. ACS Omega 7:6760–6767
10. Chiam SL, Pung SY, Yeoh FY (2020) Recent developments in MnO_2-based photocatalysts for organic dye removal: a review. Environ Sci Pollut Res 27:5759–5778
11. Jang H, Suzuki S, Miyayama M (2014) The role of Cu ions of the self-reassembled MnO_2 nanosheets for rechargeable aqueous batteries. J Eur Ceram Soc 34:4297–4304
12. Saputra E, Muhammad S, Sun H, Patel A, Shukla P, Zhu ZH, Wang S (2012) α-MnO_2 activation of peroxymonosulfate for catalytic phenol degradation in aqueous solutions. Catal Commun 26:144–148
13. Saputra E, Muhammad S, Sun H, Ang HM, Tadé MO, Wang S (2013) Different crystallographic one-dimensional MnO_2 nanomaterials and their superior performance in catalytic phenol degradation. Environ Sci Technol 47(11):5882–5887
14. Kalhor M, Samiei S, Mirshokraie SA (2021) MnO_2@Zeolite-Y nanoporous: preparation and application as a high efficient catalyst for multi-component synthesis of 4-Arylidene-Isoxazolidinone. SILICON 13:201–210
15. Cojocaru B, Neatu S, Parvulescu VI, Dumbuya K, Steinruck HP, Gottfried JM, Aprile C, Garcia H, Scaiano JC (2009) Band gap effect on the photocatalytic activity of supramolecular structures obtained by entrapping photosensitizers in different inorganic supports. Phys Chem Chem Phys 11:5569–5577
16. Aprile C, Corma A, Garcia H (2008) Enhancement of the photocatalytic activity of TiO_2 through spatial structuring and particle size control: from subnanometric to submillimetric length scale. Phys Chem Chem Phys 10:769–783
17. He K, Zhu Y, Shi H (2017) Effect of Ce-doped MnO_2 catalyst on the lithium-air battery performance in the ambient atmosphere. Ionics 23:385–393
18. Liu R, Yue L (2017) Synthesis and electrochemical properties of Co doped MnO_2 framework with nanofibrous structure. Int J Appl Ceram Technol 12:E59–E64
19. Bach S, Pereira-Ramos JP, Cachet C, Bodé M, Yu LT (1995) Effect of Bi-doping on the electrochemical behaviour of layered MnO_2 as lithium intercalation compound. Electrochim Acta 40(6):785–789
20. Lv Q, Wang S, Sun H, Luo J, Xiao J, Xiao JW, Xiao F, Wang S (2016) Solid-state thin fim supercapacitors with ultrafast charge/discharge based on N-doped-carbon-tubes/Au-nanoparticles-doped-MnO_2 nanocomposites. Nano Lett 16:40–47
21. Boyom-Tatchemo FW, Nzali S, Kamgang-Youbi G, Tiya-Djowe A, Kuete-Saa D, Acayanka E, Laminsi S, Gaigneaux EM (2017) Gliding arc plasma synthesis of MnO_2 nanorods for the plasma-catalytic bleaching of azoic Amaranth Red dye. Top Catal 60:962–972
22. Boyom-Tatchemo FW, Devred F, Ndiffo-Yemeli G, Laminsi S, Gaigneaux EM (2020) Plasma-induced reactions synthesis of nanosized α-, γ- and δ-MnO_2 catalysts for dye degradation. Appl Catal B Environ 26:118159
23. Hanon F, Hermans S, Gaigneaux EM (2024) What are the species involved in the gliding arc plasma synthesis of heterogeneous catalysts? Catal Today 430:114550
24. Mboupda AP, Acayanka E, Boyom-Tatchemo FW, Kamgang GY, Nzeufa AM, Laminsi S, Richard D (2018) New-route synthesis of N-doped TiO_2 via exposing the $TiCl_3$ precursor to non-thermal quenched plasma at various times. Mater Chem Phys 206:224–231
25. Cellier CM, Vromman V, Ruaux V, Gaigneaux EM, Grange P (2004) Sulfation mechanism and catalytic behavior of manganese oxide in the oxidation of methanetiol. J Phys Chem B 108:9989–10001
26. Cellier C, Lambert S, Gaigneaux EM, Poleunis C, Ruaux V, Eloy P, Lahousse C, Bertrand P, Pirard JP, Grange P (2007) Investigation of the preparation an activity of gold catalyst in the total oxidation of n-hexane. Appl Catal B Environ 70:406–416
27. Liu C, Wang J, Xiang L (2013) Synthesis and surface characterization of γ-MnO_2 nanostructures. J Nanomater 2013:389634
28. Zhao-di Z, Long-jun X, Jian-hang S, Wei X, Wen-li W, Chenglun L (2015) Electrochemical preparation and performance of γ-MnO_2. J Chongqing University: Eng.Ed [ISSN 1671-8224], 14:3, 79–86
29. Malankar H, Umare SS, Singh K (2009) Room temperature synthesis of Li-doped MnO_2 and its electrochemical activity. Mater Lett 63:2016–2018
30. Poonguzhali R, Gobi R, Shanmugam N, Kumar AS, Viruthagiri G, Kannadasan N (2015) Enhancement in electrochemical behaviour of copper-doped MnO_2 electrode. Mater Lett 157:116–122
31. Chen K, Pan W, Xue D (2016) Phase transformation of Ce^{3+}-doped MnO_2 for pseudocapacitive electrode materials. J Phys Chem C 120:20077–20081
32. Yuan C, Zhang Y, Pan Y, Liu X, Wang G, Cao D (2014) Investigation of the intercalation of polyvalent cations (Mg^{2+}, Zn^{2+}) into λ-MnO_2 for rechargeable aqueous battery. Electrochim Acta 116:404–412

33. Tseng LT, Lu Y, Fan HM, Wang Y, Luo X, Liu T, Munroe P, Li S, Li J (2015) Magnetic properties in α-MnO_2 doped with alkaline with elements. Sci Rep. https://doi.org/10.1038/srep09094
34. Boyom-Tatchemo FW, Devred F, Laminsi S, Gaigneaux EM (2021) Temporal post-discharge reactions effect on the oxidative catalytic properties of plasma-synthesized α-MnO_2 nanorods. Appl Catal A General 616:118109
35. Jin B, Xu L, Morein C, Chen CH, Lai M, Dharmarathna S, Dobley A, Suib SL (2010) Titanium containing γ-MnO_2 (TM) hollow spheres: one-step synthesis and catalytic activities in Li/air batteries and oxidative chemicals reactions. Adv Funct Mater 22:3373–3382
36. Jin BL, Zhang S, Liu Y, Qu F, Wu X (2016) Facile synthesis of ultralong MnO_2 nanowires as high performance supercapacitor electrodes and photocatalysts with enhanced photocatalytic activities. Cryst Eng Commun 16:9999–10005
37. Dubal DP, Dhawale DS, Gujar TP, Loklande CD (2011) Effect of different modes of electrodeposition on supercapacitive properties of MnO_2 thin films. Appl Surf Sci 257:3378–3382
38. Poonguzhali R, Shanmugam N, Gobi R, Senthilkumar A, Viruthagiri G, Kannadasan N (2015) Effect of Fe doping on the electrochemical capacitor behaviour of MnO_2 nanocrystals. J Power Sources 293:790–798
39. Mahy JG, Cerfontaine V, Poelman D, Devred F, Gaigneaux EM, Heinrichs B, Lambert SD (2018) Highly efficient low-temperature N-doped TiO_2 catalysts for visible light photocatalytic applications. Materials 11(4):584
40. Zhao S, Liu T, Javed MS, Zeng W, Hussain S, Zhang Y, Peng X (2016) Rational synthesis of Cu-doped porous δ-MnO_2 microsphere for high performance supercapacitor applications. Electrochim Acta 191:716–723
41. Cheng X, Yu X, Xing Z, Yang L (2016) Synthesis and characterization of N-doped TiO_2 and its enhanced visible-light photocatalytic activity. Arab J Chem 9:S1706–S1711
42. Yang B, Rashid S, Graham N, Yu W (2023) The impact of small organic molecules on Fe(II) coagulation: facilitating vs shielding mechanisms on charge transfer. Sep Purif 323:124424
43. Modirshahla N, Hassani A, Behnajady MA, Rahbarfam R (2011) Effect of operational parameters on decolorization of Acid Yellow 23 from wastewater by UV irradiation using ZnO and ZnO/SnO_2 photocatalysts. Desalination 271:187–192
44. Marandi R, Mahanpoor K, Sharif AAM, Olya ME, Moradi R (2013) Photocatalytic degradation of azo dye acid yellow 23 in water using NiFe2O4 nanoparticles supported on clinoptilolite as a catalyst in a circulating fludized bed reactor. J Basic Appl Sci Res 3(5):347–357
45. Ansari SA, Ansari MO, Cho MH (2016) Facile and scale up synthesis of red phosphorous-graphitic carbon nitride heterostructures for energy and environment applications. Sci Rep 6:27713
46. Ansari SA, Cho MH (2017) Facile and sustainable synthesis of carbon-doped ZnO nanostructures towards the superior visible light photocatalytic performance. New J Chem. https://doi.org/10.1039/C6NJ04070E
47. Ansari SA, Parveen N (2024) Enhanced photocatalytic degradation of organic pollutants using iron lanthanum oxide nanoparticles. MatSci Express 1(1):28–32
48. Yadav S, Jilani A, Sachan S, Kumar P, Ansari SA, Afzal M, Ansari MO (2024) Highly efficient visible-light-driven photocatalysis of rose bengal dye and hydrogen production using Ag@Cu/TiO_2 ternary nanocomposites. Chemistry 6:489–505
49. Mekprasart W, Pecharapa W (2011) Synthesis and characterization of nitrogen-doped TiO_2 and its photocatalytic activity enhancement under visible light. Energy Procedia 9:509–514
50. Boyom-Tatchemo FW, Devred F, Acayanka E, Kamgang-Youbi G, Nzali S, Laminsi S, Gaigneaux EM (2023) Effect of cation insertion on the stability of gliding arc plasma-precipitated mesoporous MnO_2 dye bleaching catalysts. J Mater Res. https://doi.org/10.1557/s43578-023-01129-z